Available online at www.sciencedirect.com

jmr&t
Journal of Materials Research and Technology

journal homepage: www.elsevier.com/locate/jmrt

Original Article

Microstructure, residual stress, and mechanical property evolution of a spray-formed vanadium-modified high-speed steel processed by post-heat treatment

Yujie Wang [a], *Shuangjie Chu* [b], *Bo Mao* [a,*], *Hui Xing* [a], *Jiao Zhang* [a,c,d,**], *Baode Sun* [a,c,d]

[a] *School of Materials Science and Engineering, Shanghai Jiao Tong University, Shanghai, 200240, China*
[b] *Baoshan Iron & Steel Cooperation Limited, Shanghai, 201900, China*
[c] *State Key Lab of Metal Matrix Composites, Shanghai Jiao Tong University, Shanghai, 200240, China*
[d] *Collaborative Innovation Center for Advanced Ship and Deep-sea Exploration, Shanghai Jiao Tong University, Shanghai, 200240, China*

ARTICLE INFO

Article history:
Received 23 December 2021
Accepted 7 March 2022
Available online 15 March 2022

Keywords:
High-speed steel
Heat treatment
Microstructure
Mechanical properties
Secondary carbide

ABSTRACT

A vanadium-modified high-speed steel (HSS) manufactured by spray forming (SF) process was subjected to different heat treatment processes and the resultant microstructural evolution and mechanical properties were investigated. In-situ high-temperature Vickers indentation associated with high-temperature tensile tests were utilized to evaluate the changes in hardness and residual stress with temperature for samples processed by annealing. Moreover, the effect of quenching temperature on hardness, bending strength and impact toughness was investigated. The secondary carbide precipitation behavior and its strengthening mechanisms were discussed in combination with transmission electron microscopy (TEM) characterization. A possible mechanism was proposed to elucidate the evolution of carbide precipitation behavior during different heat treatment processes. We envision the results gained from the present study would provide useful guidance for understanding the evolution of microstructure and mechanical properties of spray-formed HSSs processed by different heat treatment conditions and optimizing the alloy design and post–thermal mechanical processing of HSS.

© 2022 The Author(s). Published by Elsevier B.V. This is an open access article under the CC BY license (http://creativecommons.org/licenses/by/4.0/).

* Corresponding author.
** Corresponding author.
E-mail addresses: bmao@sjtu.edu.cn (B. Mao), zj119@sjtu.edu.cn (J. Zhang).

https://doi.org/10.1016/j.jmrt.2022.03.053

2238-7854/© 2022 The Author(s). Published by Elsevier B.V. This is an open access article under the CC BY license (http://creativecommons.org/licenses/by/4.0/).

1. Introduction

High-speed steels (HSSs) are widely used in the production of cutting tools and cold work tools due to their exceptional hot hardness, excellent wear resistance, high strength and good toughness [1,2]. The manufacturing process of HSSs mainly includes conventional casting (CC) [3,4], electroslag remelting (ESR) [5,6], powder metallurgy (PM) [7,8] and spray forming (SF) [9,10]. Among these processes, SF has attracted widespread attention in both industry and academia owing to its capability to produce HSS with fine microstructure with excellent near net shape ability and high flexibility [11,12]. Meanwhile, the microstructure of HSS manufactured by SF exhibits few coarse eutectic carbide networks and extremely low macrosegregation. Moreover, to further improve the engineering performance of HSS fabricated by SF, thermo-mechanical and heat treatment processes are widely utilized to optimize its microstructure and enhance mechanical properties [13,14]. Particularly, by manipulating the decomposition, and precipitation of different carbides in HSS at various stages of heat treatment processes, it is possible to tailor the mechanical properties for a variety of engineering applications. Therefore, it is extremely significant to study the microstructural evolution and mechanical properties of HSS fabricated by SF during the heat treatment process.

Due to its scientific and practical significance, the microstructural evolution of HSS processed by different heat treatment procedures has been extensively investigated, with a particular focus on the carbide precipitation behavior. For instance, the secondary carbides in spray-formed M3:2 HSS with the addition of niobium have been studied by Wang et al. [15]. The results showed that during the tempering process at 560–600 °C, fine and coherent MC and M_2C secondary carbides precipitated on the internal twin boundaries of the martensite plates and within the plates. As the tempering temperature further increased, the secondary precipitates exhibited a transformation from coarse M_3C to fine and coherent precipitates MC and M_2C [16]. As a substitutional element, Lu et al. [9] found that the addition of niobium accelerated the decomposition of M_2C carbides and increased the thermal stability of M3:2 HSS. However, due to the ultra-fine secondary carbides and poor quality of the thin foil for transmission electron microscopy (TEM) observation, these carbides with coherent transformation to the matrix cannot be imaged well after tempering [15]. Moreover, the potential of SF in terms of microstructure refinement is favorable to enhance the mechanical properties of HSS. Compared with CC HSS, the refined as-cast microstructure may lead to important improvements in the mechanical properties of HSS. Mesquita et al. [17] compared the mechanical properties of M3:2 HSS produced by SF and CC processes. The results showed that HSS fabricated by SF possesses higher isotropic toughness due to its less oriented carbide distribution. It was found that HSS processed by SF is comparable to HSS fabricated by PM in terms of microstructure, performance and isotropy [18]. Igharo et al. [19] studied the microstructure of M2 HSS deposited by SF and showed a small grain size with a cellular carbide network. No significant difference was observed between the quenching response of M2 HSS produced by CC and SF. The bending strength of SF processed M2 HSS was isotropic, similar to that observed by PM HSS. Wang et al. [16] believed that the excellent mechanical properties of M3:2 HSS fabricated by SF were pertinent to the precipitated carbides during the tempering process. It was found that secondary hardening contributed to increase the hardness and bending strength due to the fine dispersion of MC and M_2C, and the enhanced toughness was attributed to the fine precipitates and decomposition of matrix. During the over-tempering process, the hardness of M3:2 HSS was greatly reduced because of the M_2C coarsening and the precipitation of M_3C carbides [20].

Despite these research efforts, little attention has been paid to investigating the hot hardness and residual stress of HSS processed by different heat treatment processes. Hot hardness as a crucial parameter is pertinent to the mechanical performance and wear resistance of the alloy at elevated temperatures [21]. It has been proven that the quantification of hot hardness is particularly important: such as the estimation of wear resistance and fatigue limits [22,23]. Meanwhile, it is well known that residual stress has significant impacts on the mechanical properties of engineering materials, such as fatigue, fracture, corrosion, friction and wear. A recent study carried out by Li et al. [24] revealed the relationship between the porosity distribution and the residual stress of the as-sprayed tubular ASP30 HSS for the first time through neutron diffraction. However, there is still a lack of systematic analysis on the evolution of in-situ hot hardness and residual stress of spray-formed HSS and their relationship with the microstructural characteristics.

In this paper, to optimize the microstructure and mechanical properties, the vanadium-modified HSS treated by spheroidizing annealing was used. The evolution of the microstructure and mechanical properties of vanadium-modified HSS after different heat treatments was investigated in detail. We envision the results would provide useful guidance for optimizing the alloy design and post–thermal mechanical processing of HSS.

2. Experimental procedure

2.1. Materials and processing

The raw material used in this study was a vanadium-modified HSS ingot, manufactured by Heye Science and Technology Co., Ltd (China). The chemical composition is given in Table 1. The vanadium-modified HSS ingot was produced by SF process. The billet was then forged to increase the density and refine its microstructure. To optimize the microstructure and mechanical properties, forged vanadium-modified HSS was used to carry out post-heat treatment procedures. In this work, the schematic diagram of the heat treatment procedure

Table 1 – Chemical compositions of vanadium-modified HSS (wt.%).

Element	C	Cr	W	Mo	V	Si	Mn	Fe
3V-HSS	0.93	4.6	5.9	5.6	3.1	0.47	0.25	Bal.

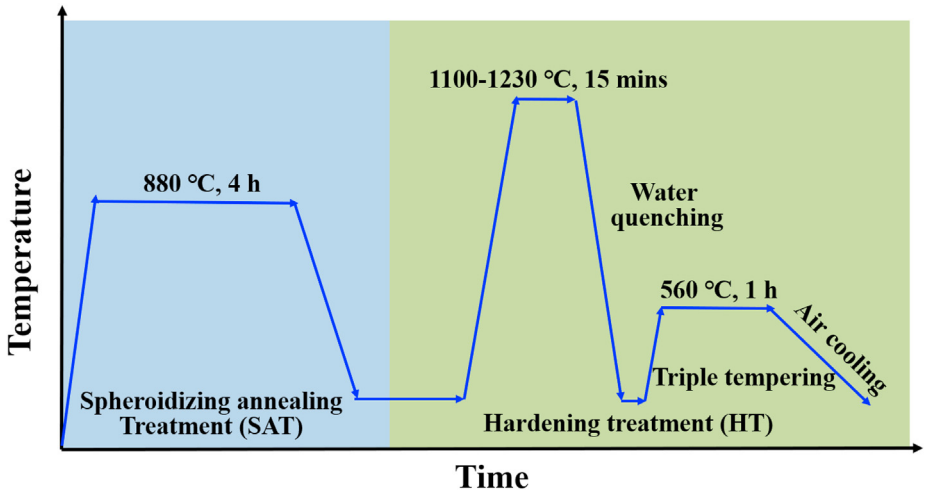

Fig. 1 – Schematic illustration of the heat treatment procedure for the HSS samples.

is shown in Fig. 1. The spheroidizing annealing treatment (SAT) was conducted by isothermally keeping the samples with a diameter of 80 mm and a length of 120 mm at 880 °C for 4 h followed by cooling in the furnace. The hardening treatment (HT) was carried out by subsequently heating the samples with a dimension of 120 × 10 × 10 mm^3 to different austenitizing temperatures (1100, 1150, 1200, and 1230 °C) for 15 min followed by water quenching. Afterwards, the samples were heated to 560 °C and held for 1 h by triple tempering. The austenitization process was carried out in a tube furnace with an argon atmosphere.

2.2. *Microstructure characterization*

To investigate the microstructural evolution of the vanadium-modified HSS during the heat treatment process, samples for metallographic inspection were prepared by standard grinding with sandpapers with grit numbers from 600 to 1500 followed by fine polishing with diamond suspensions. A field emission scanning electron microscope (SEM, JEOL JSM-7800F) was utilized to characterize the microstructural characteristics of the matrix and carbides. Image-Pro Plus 6.0 software was used to quantitatively estimate the size and volume fraction of carbides. Especially, to reduce data dispersion, three different fields of view of the same sample were selected, and the SEM images were magnified 1000 times to evaluate the size and volume fraction of carbides. Energy-dispersive X-ray spectroscopy (EDS) was employed to identify the type of carbides by analyzing the local chemical compositions. Meanwhile, electron backscatter diffraction (EBSD) observations were utilized to analyze the grain size and grain orientation maps. A step size of 1 μm was used to collect EBSD data and observe a field of view of 200 × 150 μm^2. Moreover, TEM (FEI Talos F200X) analysis was carried out to further reveal the fine structure and crystallographic relationship between the matrix and carbide precipitation. Thin foil samples for TEM characterization were prepared by mechanical grinding to a thickness below 50 μm followed by ion milling (Gatan 691).

2.3. *Mechanical property evaluation*

The mechanical properties of the SAT and HT-processed HSS samples were evaluated by a variety of mechanical testing. To evaluate the surface residual stress and hot hardness of SAT-processed samples, in-situ high-temperature microhardness tests were carried out by utilizing a Vickers indentation (HTV-PHS30) machine. Especially, the detailed procedures and mechanisms for measuring the residual stress through indentation techniques are shown in the supplementary materials. The micro-hardness tests were conducted at temperatures of 25 °C, 300 °C, 400 °C, 500 °C, 560 °C, 600 °C and 650 °C. The specimen size was 8 × 4 × 3 mm^3, and the heating rate was 50 °C/min. The test was repeated five times at different temperatures with a load of 1 kg and a dwelling time of 15 s. Argon gas was introduced into the chamber of the Vickers indentation machine during the tests to prevent the sample surface from oxidation. After microhardness tests, the indentation morphologies on the samples were examined in SEM and analyzed by Image-Pro Plus 6.0 software. Moreover, high-temperature tensile tests were carried out on a universal testing machine (Zwick/Roell Z050) to evaluate the yield stress and correlate the residual stress of SAT-processed HSS samples. Dog-bone specimens with a gauge length of 15 mm, a width of 4 mm, and a thickness of 2 mm were used for tensile tests. The test temperatures were adjusted corresponding to the in-situ high-temperature Vickers indentation experiments. Samples for high-temperature tensile tests were firstly heated to the target temperature and kept for 5 min. Afterwards, uniaxial loadings were applied at a constant rate of 1 mm/min until fracture of the samples. Each test was repeated 3 times and the stress–strain data was recorded. It is necessary to emphasize that although hardness and tensile testing dwell times were different, microstructural changes were not expected at such temperatures and shorter exposure times. In the field application of HSS, the cutting-edge of the tool experiences higher temperature under severe loading condition. Therefore, microstructural stability is required.

To elucidate the effect of austenitizing temperature on the microstructure and mechanical properties of HT-processed samples, three-point bending fracture tests were performed at a bending rate of 1 mm/min for a total of 24 specimens. The dimension of the tested samples was 40 (length) × 5 (width) × 5 (height) mm^3 and the span was 20 mm. Moreover, impact toughness tests were carried out on 24 unnotched specimens with dimensions of 55 (length) × 10 (width) × 10 (height) mm^3 according to ISO 5754 [25]. Micro-hardness tests of HT-processed samples were also conducted with the same testing conditions as SAT-processed samples.

3. Results

3.1. *Microstructure, hot hardness and residual stress of SAT-processed HSS*

The solidification sequences and phase transformation of vanadium-modified HSS were calculated by Thermo-Calc software (TCFE7 database). Fig. 2 shows the calculated results of Fe–6W–5Mo–4Cr–3V–C, in which the red dashed section represents the evolution of the phase diagram of the HSS in this paper under equilibrium. It can be seen that as the temperature decreases, M_6C and MC carbides are gradually precipitated. The calculated diagram shows the carbides M_6C and MC as stable ones. The predicted results provide useful guidance for subsequent experimental observation and analysis.

SAT process plays a significant role on the manufacturing process of HSS. First, machining of HSS components is often finished just after the SAT process due to its capability to reduce the hardness and make HSS in a softer state [26]. Moreover, extensive research efforts have revealed that the distribution and morphology of the main carbides would not change too much after HT process. Direct inspection of eutectic carbide inhomogeneities during the annealed condition shows consistent results during the quenched and tempered condition. In this regard, the microstructure of the HSS processed by SAT process somehow significantly affect the final microstructure of HSS [27]. Fig. 3 shows the microstructural details of SAT-processed vanadium-modified HSS. It can be seen that primary carbides and dispersed granular secondary carbides are distributed in the matrix, as shown in Fig. 3(a). A large number of white and gray carbide particles are dispersed in the matrix, and the difference in the contrast value indicates that there are at least two types of carbides. To further identify the type of carbides, close-up areas of different carbides were used for EDS analysis, as shown in Fig. 3(b and c). It can be found that SAT-processed HSS is rich in vanadium, tungsten and molybdenum carbides. Based on the EDS results, the stoichiometry of these carbides is identified as MC (gray) and M_6C (white), respectively. Meanwhile, through the statistical calculation of Image-Pro Plus 6.0, the volume fractions of MC and M_6C carbides are estimated to be 5.05 ± 1.27% and 6.26 ± 0.73%. Correspondingly, the average sizes are 6.32 ± 1.54 μm and 4.07 ± 1.60 μm, respectively. In particular, it is emphasized that the quantification of the volume fraction of carbides is mainly primary carbides, and almost excludes secondary carbides due to the size limitation. EBSD analysis of the SAT-processed vanadium-modified HSS in Fig. S1 reveals that the microstructure shows an average grain size of 9.2 μm and no preferential crystallographic texture is observed.

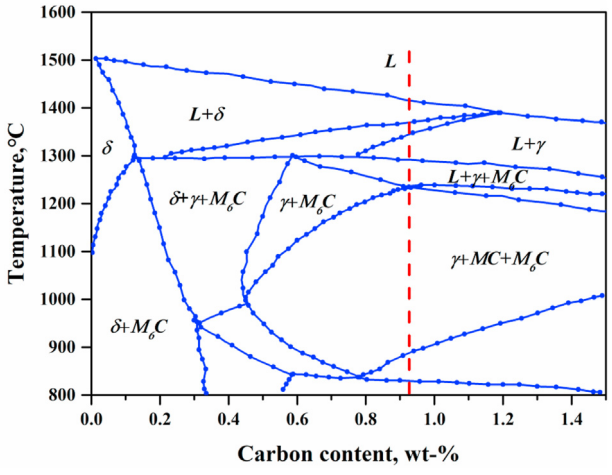

Fig. 2 – Pseudobinary sections were calculated using Thermo-Calc.

The SEM images and quantitative analysis results of the indentation morphologies of SAT-processed samples after micro-hardness tests are shown in Fig. 4. Fig. 4(a) shows the indentation surface morphology of the sample after the micro-hardness test at room temperature. It can be seen that a diamond indentation was left on the sample surface. A closer check of the indentation reveals that there is some discrepancy between the ideal projected contact area and the real contact area, which can be utilized as an indication for the state and magnitude of the residual stress. The peripheries of the ideal and real contact areas were marked by the yellow and red lines, respectively. A quantitive measurement of the real contact area, A_C, and the nominal projected area, A_{nom}, was carried out and the ratio of A_C to A_{nom}, denoted C^2, was calculated. A similar analysis was also conducted on the SAT-processed samples after micro-hardness performing at temperatures of 300 °C (Fig. 4(b)), 400 °C (Fig. 4(c)), 500 °C (Fig. 4(d)), 560 °C (Fig. 4(e)), 650 °C (Fig. 4(f)). Compared with Fig. 4(a), the discrepancy between the ideal projected contact area and the actual contact area seems to become more prominent. The corresponding values C^2 were calculated and shown in each figure. For instance, in Fig. 4(c), $C^2 = 0.9554$ at $T = 400$ °C, and then reduce to $C^2 = 0.9426$ at $T = 500$ °C, as shown in Fig. 4(d). Meanwhile, $C^2 = 0.9376$ at $T = 560$ °C in Fig. 4(e), and then reach the minimum value $C^2 = 0.9213$ at $T = 650$ °C, as depicted in Fig. 4(f). For 400 °C ≤ T ≤ 650 °C, C^2 values continue to decrease because the difference between A_{nom} and A_C tends to increase, which is responsible for the inherent softening and plastic deformation of SAT-processed HSS at elevated temperatures.

Moreover, the stress–strain relationship of SAT-processed HSS at different test temperatures is shown in Fig. 5. It can be seen that the yield stress of SAT-processed HSS has a strong dependence on the test temperature. As the test temperature increases, the yield stress of HSS gradually decreases. For instance, the yield stress at $T = 25$ °C is 410 ± 7.7 MPa. As the test temperature increases to 650 °C, the yield stress dramatically drops to 185 ± 9.5 MPa. Therefore, by extracting

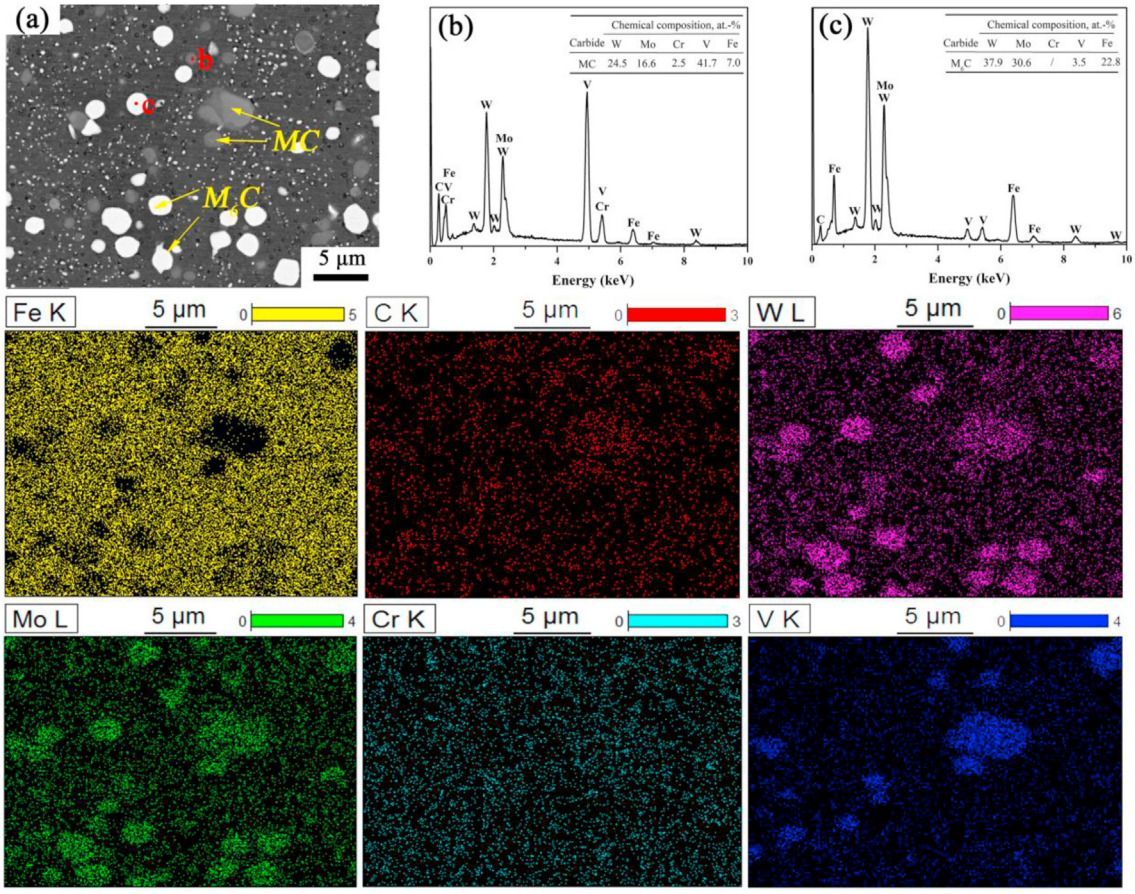

Fig. 3 – SEM microstructure observations of SAT-processed HSS, (b) EDS of the gray particles in (a), and (c) EDS of the white particles in (a), EDS mapping corresponds to the entire region in Fig. (a).

the yield stress data of SAT-processed HSS, the residual stress of HSS was calculated and is plotted together with the hardness as a function of test temperature, as shown in Fig. 6. It can be seen that after spheroidizing annealing, the hardness of SAT-processed HSS is 230.3 ± 6 HV at room temperature. At $T = 300$ °C, its value drops to 195 ± 4.8 HV. Subsequently, when the test temperature exceeds 300 °C, the hardness of SAT-processed HSS decreases slightly and reduces to 163 ± 2.6 HV at $T = 650$ °C. Correspondingly, it can be found that the changing trend of SAT-processed HSS residual stress is the opposite. For 25 °C ≤ T ≤ 400 °C, the residual stress of SAT-processed HSS increases with the increase of test temperature. The residual stress reaches the maximum value of 62.6 ± 1.9 MPa at $T = 400$ °C. When $T > 400$ °C, the residual stress of SAT-processed HSS gradually reduces to 43.6 ± 2.3 MPa at $T = 650$ °C. It should be noted that the low residual stress in this study is attributed to the elimination of spheroidizing annealing, which also shows the effectiveness of the heat treatment process.

3.2. *Microstructure and mechanical properties of HT-processed HSS*

SEM and EDS characterization were performed to further reveal the microstructure of HT-processed HSS and the results are shown in Fig. 7. It can be seen that the microstructure consists of tempered martensite, together with primary carbides MC, M_6C and dispersed nano-scale secondary carbides distributed within grains or at the grain boundaries. As mentioned earlier, MC is identified as gray blocks and M_6C is characterized as the white particles, which indicates that there is no obvious change in phases after triple tempering, as shown in Fig. 7(a). Meanwhile, a considerable amount of the small secondary carbides can be observed within the microstructure. As the quenching temperature increases, there is no significant change in the size and distribution of the MC and M_6C, as shown in Fig. 7(b) and (c). EDS analysis was performed on a selected area in Fig. 7(c') and the element mapping analysis also demonstrates that the type of primary carbides has not changed after tempering. Whereas the density of small secondary carbides decreases with the austenitizing temperature, which is observed by the negligible secondary carbides in Fig. 7(d). This is probably related to the slower decomposition and diffusion of alloy carbides caused by the lower quenching temperature, because M_6C begins to dissolve at higher than 1037 °C, MC begins to dissolve above 1100 °C, and the dissolution rate of MC is slower than that of M_6C [28]. Chaus et al. [29] believed that this fact can be ascribed to the increasing stability of the austenite affected by increasing austenitizing temperature that could result in the less intensive secondary carbide precipitation from both the retained austenite and martensite during tempering at $T = 560$ °C.

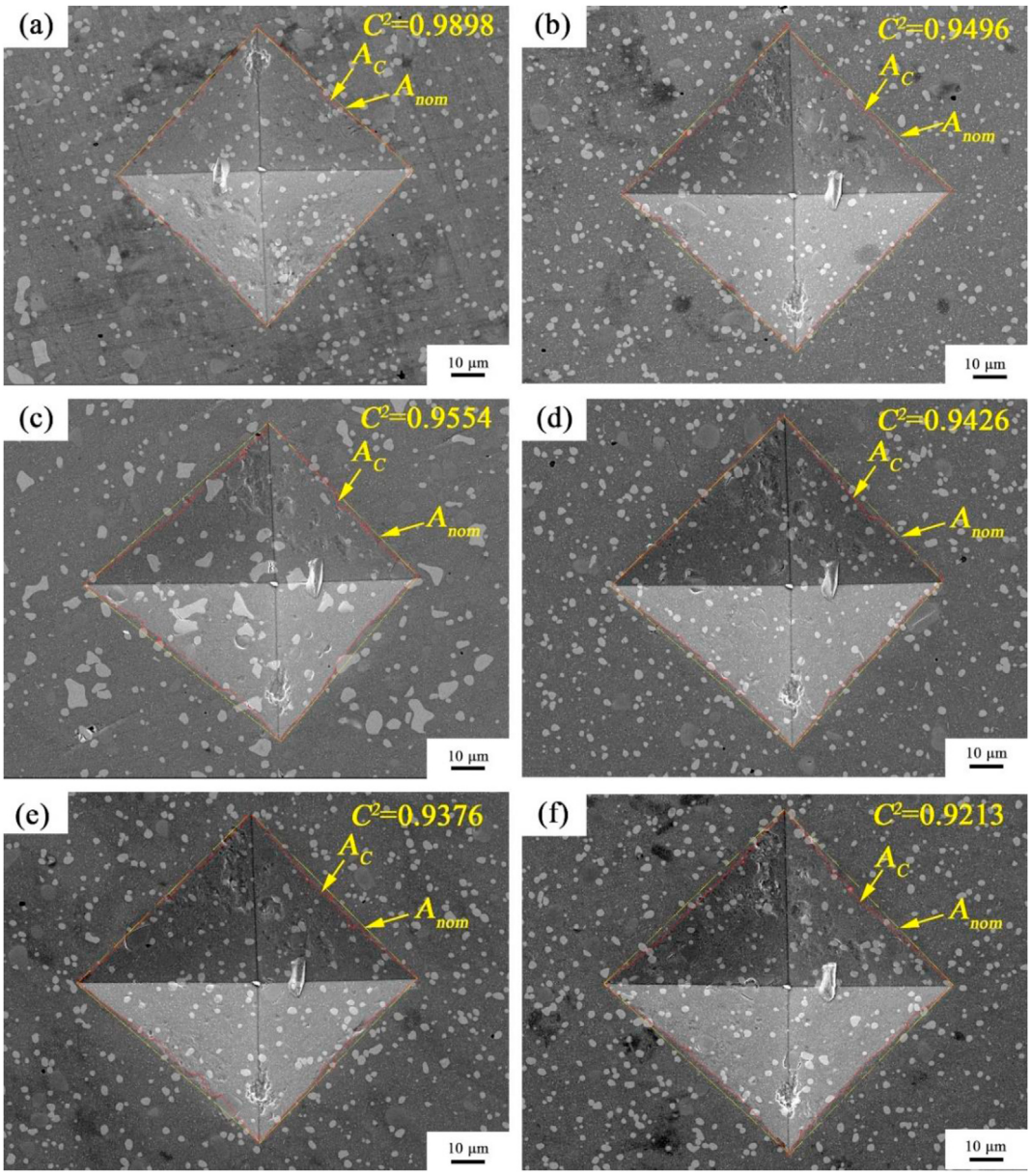

Fig. 4 – SEM images of the surface morphologies of the SAT-processed HSS after in-situ high temperature indentation at temperatures of (a) 25 °C, (b) 300 °C, (c) 400 °C, (d) 500 °C, (e) 560 °C, and (f) 650 °C.

Moreover, quantitative measurement of the size and volume fraction of carbides was also performed by analyzing the SEM images through Image-Pro Plus software and the results are shown in Table 2. It can be seen that the average volume fractions of primary carbides MC and M_6C are 6.11 ± 1.00% and 5.69 ± 0.20% as the quenching temperature is 1100 °C, respectively. As the quenching temperature increases to 1230 °C, the volume fractions of MC and M_6C are 4.68 ± 0.20% and 6.75 ± 0.30%, indicating the insignificant effect of the quenching temperature on the primary carbides. This fact strongly indicates that the total volume fraction of eutectic carbides and the volume fraction of each different eutectic carbide are mainly pertinent to the chemical composition [30,31]. As the quenching temperature increases, the dissolved carbides in the austenite increases. Therefore, the volume fraction of carbides decreases with the austenitization temperature, which can be evidenced from previous studies [32,33]. However, the undissolved carbides may grow slightly during the quenching process, leading to the gradual decrease of the fine carbides and increase of the large carbides. Liu et al. [34] found that the volume fraction of carbides follows a decrease, increase, and then decreases with the increase of the quenching temperature, which is consistent with the results in the present study.

The evolutions of the mechanical properties of HT-processed HSS as a function of quenching temperature are plotted in Fig. 8. Fig. 8(a) describes the effects of various austenitizing temperatures on the bending strength of HT-processed HSS. It is found that the bending strength does not change monotonously with increasing quenching temperature. It can be seen that HT-processed HSS exhibits the maximum bending strength after quenching at $T = 1200$ °C

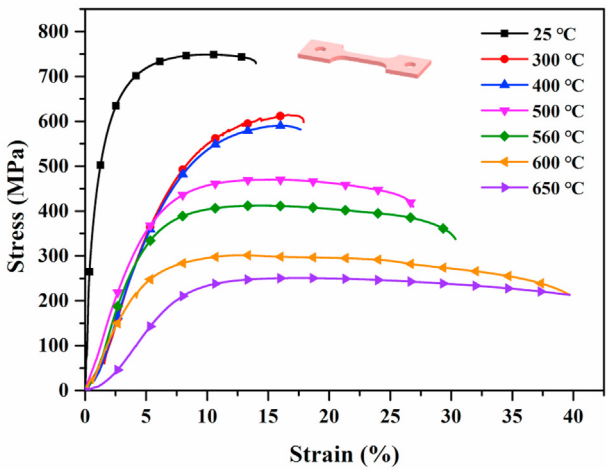

Fig. 5 – Engineering stress–strain curves of SAT-processed HSS identified by tensile tests under elevated temperatures.

and tempering at $T = 560$ °C, which is 4258 ± 412 MPa. After continuing to increase the quenching temperature, it can be seen that the bending strength is the lowest within the range of the studied heat treatment procedure, which is 2649 ± 136 MPa. In particular, after quenching at $T = 1100$ °C and $T = 1150$ °C together with tempering at $T = 560$ °C, respectively, there is no significant variation for the bending strength of HT-processed HSS. Meanwhile, the effects of different austenitizing temperatures on the impact toughness and Vickers hardness of HT-processed HSS are displayed in Fig. 8(b). It can be seen that the impact toughness and Vickers hardness show a monotonous decrease and increase tendency with increasing quenching temperature, respectively. It can be found that the impact toughness gradually decreases within the range of the heat treatment procedure. For instance, the maximum impact toughness is 65.7 ± 9 J at $T = 1100$ °C. By contrast, at $T = 1230$ °C, the minimum impact toughness decreases to 29.8 ± 6.1 J. In addition, the Vickers hardness of HT-processed HSS continues to rise with the increase of quenching temperature. It changes from 611 ± 5 HV at $T = 1100$ °C to 881 ± 14 HV when quenching $T = 1230$ °C.

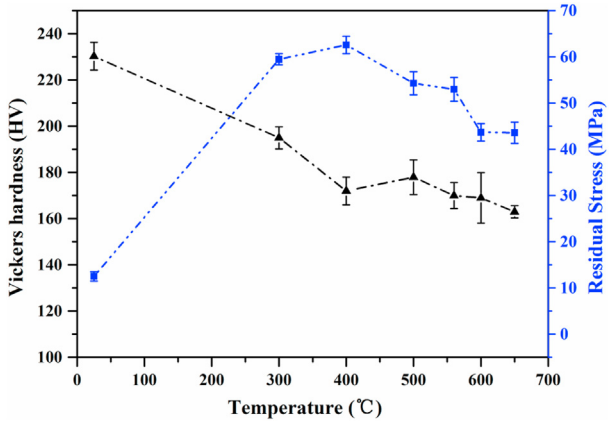

Fig. 6 – Evolution of Vickers hardness and residual stress of SAT-processed HSS as a function of test temperature.

4. Discussion

4.1. *Evolution of hot hardness and residual stress of SAT-processed HSS*

Hot hardness plays a key role during the engineering applications of HSS and is significantly affected by the type, distribution, and morphology of the carbides in its microstructure. From Fig. 6, it can be found that the downward trend of the hot hardness is slowly within the tested temperature range, which is pertinent to the existence of abundant alloy carbides and high-temperature stable elements (such as molybdenum) in HSS. It was reported that alloy carbides could compensate for the hardness level at high temperatures due to their higher mechanical strength [35]. Meanwhile, the involved molybdenum element delays the high temperature softening [21]. It can be inferred that SAT-processed HSS has a relatively stable hardness level due to the uniform microstructure (See the Supplementary materials Fig. S1) and abundant carbides at different temperatures.

Moreover, the softening behavior of steels with increased temperature has been accounted for by several different mechanisms, such as the dissolution of precipitates [36]; over-ageing of precipitates [37]; dislocation rearrangement leading to the formation of dislocation sub-grain structure with lower internal stress [38]; dislocation slip and deformation twinning (up to 0.5 T_m, T_m is melting point) [39]. Based on the aforementioned factors, the test temperature and time in our case are not enough to dissolve smaller carbides and grow larger carbides. Therefore, as $T \leq 400$ °C, it can be inferred a deformation regime exists, and the yield stress below 400 °C increases rapidly with the decrease in temperature due to lattice resistance to dislocation slip [21]. For 400 °C < T < 650 °C, it was reported that the decrease in hardness is attributed to creep at $T > (0.3–0.4)\ T_m$ (T_m is estimated to be 1407 °C in our case by Jmatpro software) [21]. This rate-dependent plastic deformation is considered to be dominant at $T > 0.4\ T_m$, is likely controlled by dislocation climb aided by increased lattice diffusion at high temperatures [40]. Regarding the phenomenon that the hardness at 500 °C is higher than 400 °C, which is probably HSS under short-term deformation at high temperatures can be hardened due to easy dislocation proliferation and cross-slip, and at the same time can recover due to recrystallization, or dislocation annihilation and rearrangement [41]. Hardening and recovery offset each other at once during high-temperature deformation, so that elastic–plastic deformation proceeds in balance. However, in this specific temperature range, the offset and the balance no longer occur, hardening dominates recovery. Consequently, the HSS is strengthened [41].

One salient feature Fig. 6 is the gradual increase and then decreasing of the residual stress with temperature, showing a peaking phenomenon. To clarify the residual stress state, the stress-sensitive indentation contact morphologies are modeled, as illustrated in Fig. 9. Based on sinking-in ($C^2 < 1$) or piling-up ($C^2 > 1$), it can be found that $C^2 < 1$ at various temperatures in Fig. 4, indicating that the surface residual stress of SAT-processed HSS is a tensile stress state. The previous study has shown that the hardness increases with the

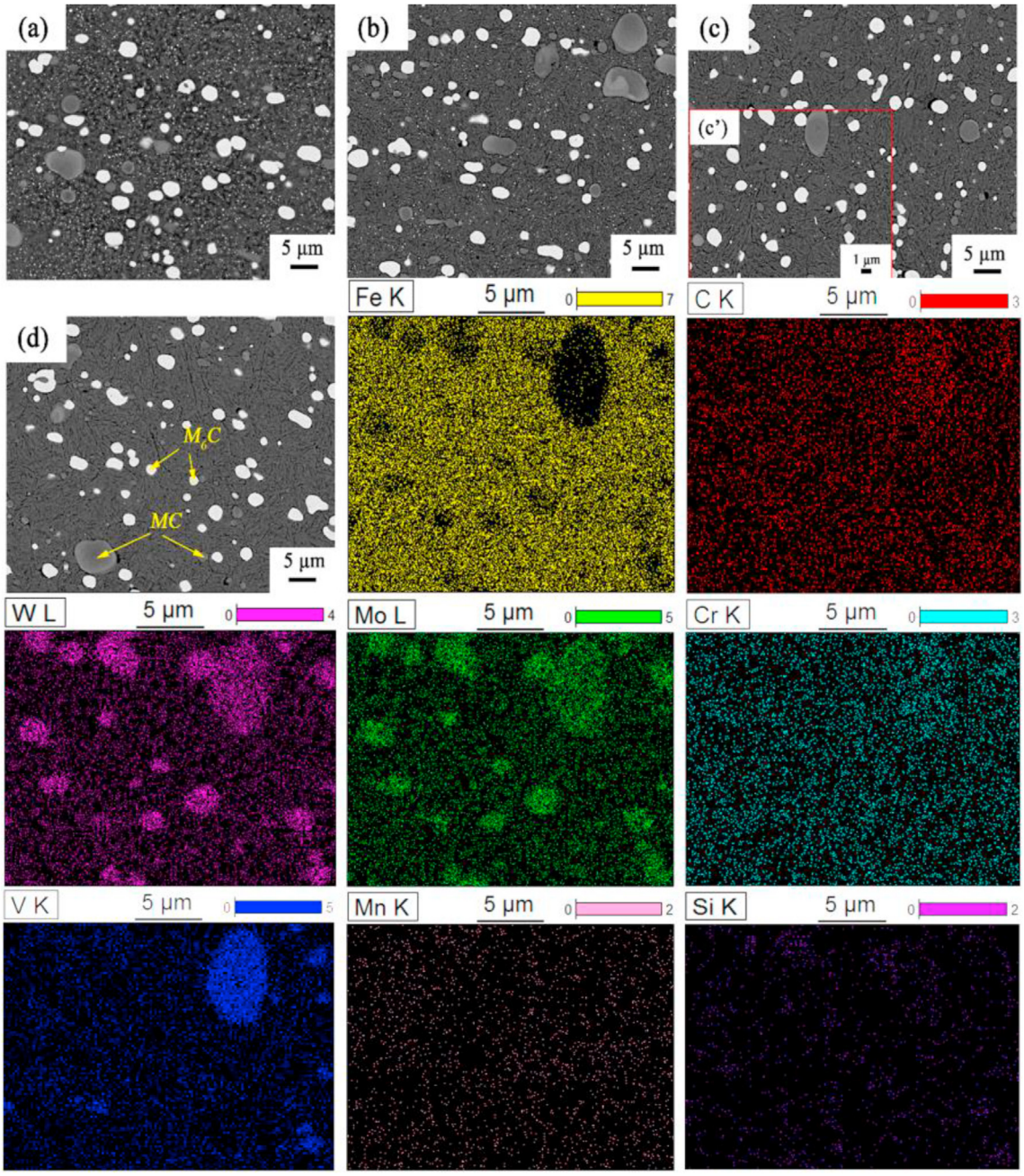

Fig. 7 – Typical SEM micrographs of HT-processed HSS under different austenitizing temperatures, (a) 1100 °C, (b) 1150 °C, (c) 1200 °C, (d) 1230 °C, where (c') corresponds to EDS mapping, respectively.

compressive residual stress and decreases with the tensile residual stress [42], which is in good agreement with the evolution trend of Fig. 6. In the presence of tensile stress, the pileup is small but sinking. In terms of piling-up or sinking-in behavior, the study believed that it was pertinent to the hardening behavior (n) and yield strain (σ_y/E) [43]. For higher yield strain, only sinking-in occurs, while for smaller values, piling-up or sinking-in may occur [44]. It is necessary to emphasize that the accuracy of residual stress evaluation depends on material properties, friction coefficient, or indenter tip radius, among which strain hardening behavior is the main factor that causes the nonlinear effect of residual stress on the indentation response [45–47]. Since the influence of friction coefficient and indenter tip radius is almost invariable for a specific indenter in our case, it can be concluded that the evolution of residual stress is mainly related to material properties. Therefore, it can be inferred that the hardening behavior and yield strain of SAT-processed HSS at high temperatures affect the change of residual stress.

4.2. *Effect of austenitizing temperature on mechanical properties of HT-processed HSS*

Austenitizing temperature has a significant impact on the secondary carbide distribution and mechanical properties of HSS. During the austenitizing and quenching process,

Table 2 – Average size and volume fraction of primary carbides of HSS after annealing and tempering.

Conditions	Volume fraction (%)		Average size (μm)	
	MC	M_6C	MC	M_6C
Annealing	5.05 ± 1.27	6.26 ± 0.73	6.32 ± 1.54	4.07 ± 1.60
1100@560	6.11 ± 1.00	5.69 ± 0.20	4.77 ± 0.81	2.98 ± 0.56
1150@560	6.08 ± 0.63	6.36 ± 0.23	4.93 ± 1.52	2.66 ± 0.52
1200@560	4.60 ± 0.75	6.26 ± 0.40	6.83 ± 0.21	2.79 ± 0.51
1230@560	4.68 ± 0.20	6.75 ± 0.30	6.32 ± 0.08	3.17 ± 0.07

secondary carbides dissolve in the austenite and precipitate again. The higher the austenitizing temperature, the more secondary carbide dissolves. Therefore, the more alloy carbides dissolve in the austenite, resulting in the precipitation of more fine carbides in the tempered martensite matrix at an elevated quenching temperature [48]. Together with the high density of dislocations induced by martensitic transformation, the bending strength and microhardness of HT-processed HSS gradually increase, as shown in Fig. 8 [5]. However, an abnormal phenomenon exists when the quenching $T = 1230$ °C, the decrease in bending strength is probably due to more carbides dissolved into the austenite, and there are not enough carbides to pin the grain boundaries, which promotes the growth of grains and results in wider martensite lath after tempering. On the contrary, the stability of retained austenite increases with decreasing quenching temperature, resulting in more retained

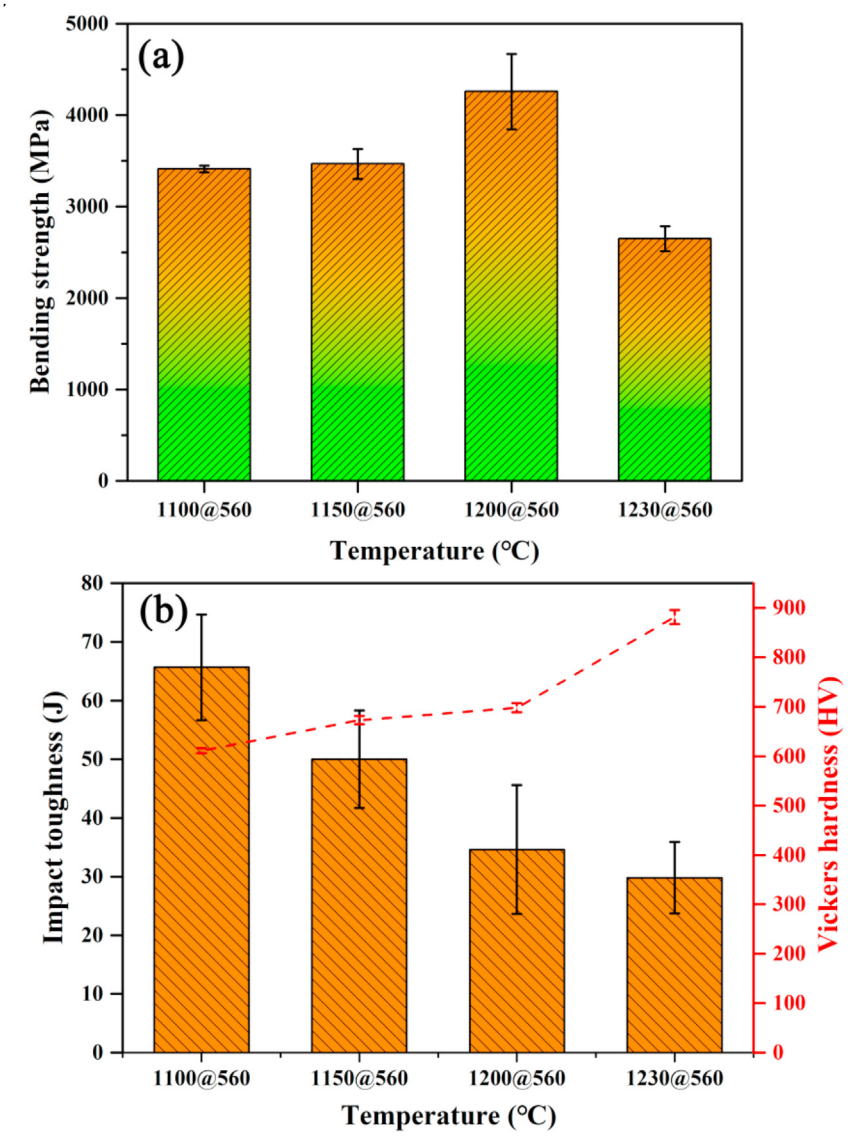

Fig. 8 – Evolution of mechanical properties of HT-processed HSS under different austenitizing temperatures, (a) bending strength, (b) impact toughness and Vickers hardness.

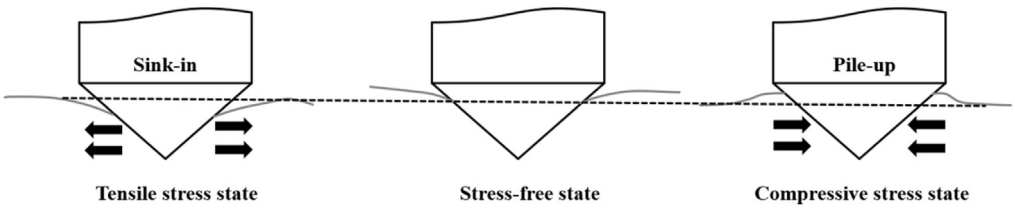

Fig. 9 – Effect of residual stress on the contact morphology of indentation in the loaded state.

austenite contributing to higher impact toughness, as shown in Fig. 8(b). Furthermore, as shown in Table 2, the influence of carbide size on impact toughness may be more significant than carbide distribution [49].

Taking into account the same tempering conditions, HT-processed HSS indicates exceptional high microhardness at the quenching $T = 1230$ °C. To further elucidate the contribution of secondary carbides to mechanical properties during the tempering process, TEM observation was performed after quenching at $T = 1230$ °C and tempering at $T = 560$ °C, as shown in Fig. 10. As expected, it can be seen that the secondary carbide particles MC and M_6C are distributed in the martensite matrix, and the measured sizes are approximately 224 nm and 302 nm, respectively, as shown in Fig. 10(a). The bright and dark field images of considerably finer carbide particles, together with selected area electron diffraction patterns are illustrated in Fig. 10(b and c), respectively. It can be seen that finer carbide particles are dispersed in the martensite.

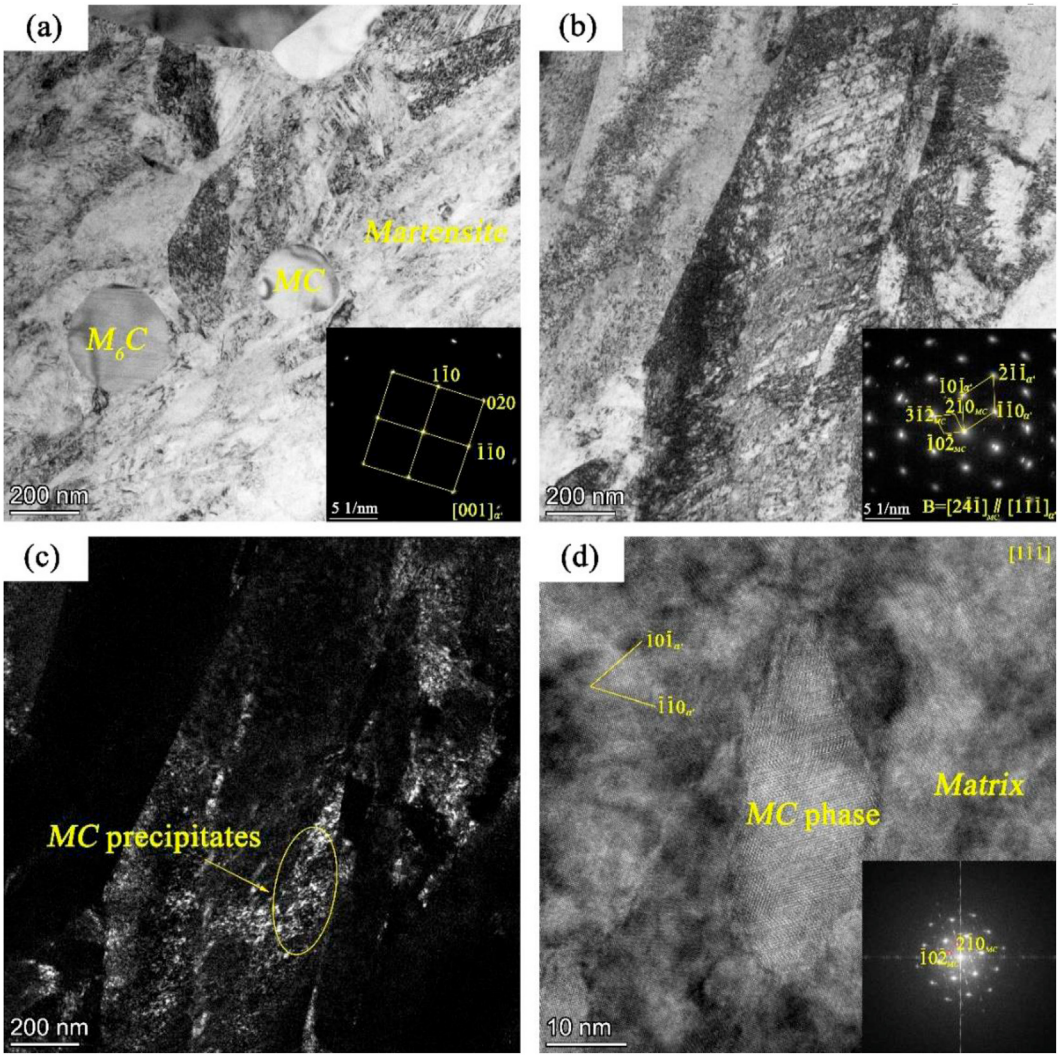

Fig. 10 – Secondary precipitation of MC in plate martensite of HT-processed HSS at austenitizing $T = 1230$ °C, (a, b) bright field, (c) dark field, (d) HRTEM image of MC carbides precipitated at the matrix in HT-processed HSS, the inset in d is the corresponding FFT image.

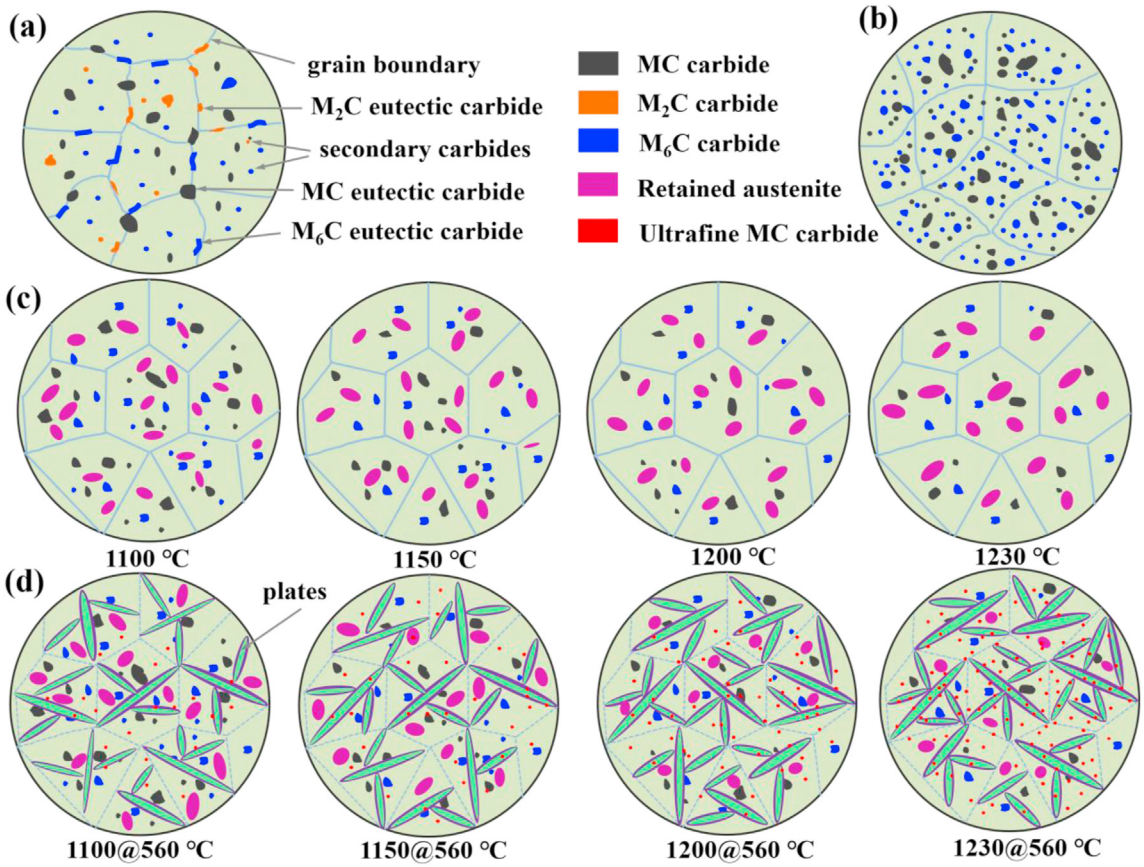

Fig. 11 – Schematic diagram of microstructural evolution of vanadium-modified HSS, (a) as-sprayed state, (b) after spheroidizing annealing, (c) quenched at 1100–1230 °C, (d) tempered at 560 °C.

Especially, using selected area diffraction patterns and lattice parameter measurement to calibrate the finer carbide particles, it is considered that the fine carbide particles are MC-type secondary carbide, and its stoichiometry is likely to be V_8C_7. The estimated length of fine MC secondary precipitate is approximately 45 nm by high-resolution transmission electron microscopy (HRTEM), and the inset is the corresponding fast Fourier transformation (FFT) image, as shown in Fig. 10(d). It can be observed that the fine MC precipitate is embedded in the martensite matrix. It should be emphasized that the secondary carbides mainly affect the hardness of HSS, which can be attributed to their ability to be easily dissolved during the austenitization process [29]. Consequently, it is demonstrated that secondary MC precipitates are the principal factor affecting the hardness of HT-processed HSS. Moreover, the study of Hetzner et al. suggested that disc-shaped MC and needle-shaped M_2C usually precipitate in tempered HSS [50]. However, M_2C carbide failed to observe by TEM in this study due to differences in manufacturing routes and heat treatment procedures [51], and similar observations have also been found in other available data [8,52].

Especially, the origin of secondary carbides precipitated is still an open question, which has been evidenced by Boccalini and Goldstein [51], Ghomashchi and Sellars [53], as well as Chaus and and Dománková [29,48]. To clarify some misunderstandings and statements, it is necessary to more accurately grasp the formation mechanism of carbides to avoid conflicting uses with the same expression. Based on the experimental observation in our study, a possible mechanism was proposed to account for the precipitation behavior of HSS as processed by different heat treatments and the schematic illustration is shown in Fig. 11. The solidification microstructure of vanadium-modified HSS manufactured by SF process is shown in Fig. 11(a). Different from the microstructure of HSS fabricated by CC, the microstructure of HSS produced by SF is composed of equiaxed grains, discontinuous and significantly refined eutectic carbide network distributed at the grain boundaries and within the matrix. These eutectic carbides are marked with different symbols and colors in Fig. 11(a). The type, morphology, volume fraction and size of eutectic carbides vary significantly with the chemical composition of HSS and the cooling rate during solidification [29,48]. In addition to eutectic carbides, the so-called secondary carbides are formed in residual δ ferrite or supersaturated austenite through a eutectoid transformation during solidification [54]. During the spheroidizing annealing, the secondary carbides are dispersed in the matrix, as shown in Fig. 11(b). The M_2C carbide, being metastable, decomposes into MC and M_6C carbides when heated to 900–1150 °C [51]. In this work, the absence of M_2C is considered to be caused by decomposition during high-

temperature hot forging. Afterwards, eutectoid transformation occurs during the cooling process, and secondary carbide particles are precipitated with a size of about 200–500 nm [55]. After quenching, the HSS microstructure consists of quenched martensite, retained austenite and undissolved carbides, as shown in Fig. 11(c). It should be emphasized that this work believes that a small number of secondary carbides in the microstructure are not dissolved, which leads to inheritance in the tempered microstructure instead of the precipitated carbides. This fact can be demonstrated from the analysis of Figs. 7 and 8. Extremely fine nanoscale secondary carbides are precipitated in the martensite during tempering, as shown in Fig. 11(d). It is worth noting that different from the aforementioned secondary carbides, the origin of these carbides is different, and the size is less than 100 nm. In this work, the size of the extremely fine secondary carbides is approximately 45 nm, which is consistent with the 10–40 nm measured by Chaus and Dománková [29]. In general, the precipitation process is strongly controlled by the diffusion and redistribution of carbon and alloying elements, as well as their mass transfer between the matrix and the secondary carbides.

5. Summary and conclusions

The microstructural evolution and mechanical properties of spray-formed vanadium-modified high-speed steel (HSS) under different heat treatment conditions were investigated and discussed. The main conclusions can be summarized as follows:

(1) The microstructure of spheroidizing annealing treatment (SAT)-processed HSS consists of pearlite and granular carbides. In-situ high-temperature indentation results show that hot hardness decreases with increasing test temperature, which is ascribed to the surface softening of SAT-processed HSS at elevated temperatures. Meanwhile, the surface residual stress of SAT-processed HSS is a tensile stress state evaluated by the indentation method.
(2) The experimental results of the mechanical properties of hardening treatment (HT)-processed HSS show that the microhardness increases monotonously with the increase of the quenching temperature, the bending strength reaches the maximum value at $T = 1200\ ^{\circ}C$, and the impact toughness decreases monotonously.
(3) Transmission electron microscopy (TEM) observation suggests that numerous nano-scale MC carbides are the main factors affecting the hardness of HT-processed HSS. A possible mechanism is proposed to elucidate the evolution of carbide precipitation behavior during different heat treatment processes.

Declaration of Competing Interest

The authors declare that they have no known competing financial interests or personal relationships that could have appeared to influence the work reported in this paper.

Acknowledgments

Tohis work has been supported by the Technology and Engineering Center for Space Utilization, the Chinese Academy of Sciences, the National Natural Science Foundation of China (Nos. 52101046, 51627802, 51821001) and the National Key Research and Development Program of China (No. 2020YFB0311200).

Appendix A. Supplementary data

Supplementary data to this article can be found online at https://doi.org/10.1016/j.jmrt.2022.03.053.

REFERENCES

[1] Kim CK, Kim YC, Park JI, Lee S, Kim NJ, Yang JS. Effects of alloying elements on microstructure, hardness, and fracture toughness of centrifugally cast high-speed steel rolls. Metall Mater Trans 2005;36(1):87–97.
[2] Pirtovšek TV, Kugler G, Godec M, Terčelj M. Three important points that relate to improving the hot workability of ledeburitic tool steels. Metall Mater Trans 2012;43(10):3797–808.
[3] Fu H, Xiao Q, Xing J-D. A study on the crack control of a high-speed steel roll fabricated by a centrifugal casting technique. Mater Sci Eng, A 2008;474(1–2):82–7.
[4] Chaus A, Bračík M, Sahul M, Dománková M. Microstructure and properties of M2 high-speed steel cast by the gravity and vacuum investment casting. Vacuum 2019:162183–98.
[5] Luo YW, Guo HJ, Sun XL, Guo J, Wang F. Influence of tempering time on the microstructure and mechanical properties of AISI M42 high-speed steel. Metall Mater Trans 2018;12:5976–87. 49A5976-86.
[6] Luo YW, Guo HJ, Sun XL, Guo J. Influence of the nitrogen content on the carbide transformation of AISI M42 high-speed steels during annealing. Sci Rep 2018;8(1):4328.
[7] Chen N, Luo R, Xiong H, Li Z. Dense M2 high speed steel containing core-shell MC carbonitrides using high-energy ball milled M2/VN composite powders. Mater Sci Eng 2020;771(13):1–9.
[8] Peng H, Hu L, Li L, Zhang L, Zhang X. Evolution of the microstructure and mechanical properties of powder metallurgical high-speed steel S390 after heat treatment. J Alloys Compd 2018:740766–73.
[9] Lu L, Hou LG, Zhang JX, Wang HB, Cui H, Huang JF, et al. Improved the microstructures and properties of M3:2 high-speed steel by spray forming and niobium alloying. Mater Char 2016:1171–8.
[10] Zhao SL, Fan JF, Zhang JY, Chou KC, Le HR. High speed steel produced by spray forming. Adv Manuf 2016;4(2):115–22.
[11] Grant P. Spray forming. Prog Mater Sci 1995;39(4–5):497–545.
[12] Grant P. Solidification in spray forming. Metall Mater Trans 2007;38(7):1520–9.
[13] Schulz A, Uhlenwinkel V, Escher C, Kohlmann R, Kulmburg A, Montero MC, et al. Opportunities and challenges of spray forming high-alloyed steels. Mater Sci Eng, A 2008;477(1–2):69–79.
[14] Zhang G, Yuan H, Jiao D, Li Z, Zhang Y, Liu Z. Microstructure evolution and mechanical properties of T15 high speed steel prepared by twin-atomiser spray forming and thermo-mechanical processing. Mater Sci Eng, A 2012:558566–71.

[15] Wang H, Hou L, Zhang J, Lu L, Cui H. The secondary precipitates of niobium-alloyed M3:2 high speed steel prepared by spray deposition. Mater Char 2015:106245–54.
[16] Wang H, Hong D, Hou L, Ou P, Zhao H. Influence of tempering temperatures on the microstructure, secondary carbides and mechanical properties of spray-deposited AISI M3:2 high-speed steel. Mater Chem Phys 2020;255:123554. 2551-11.
[17] Mesquita RA, Barbosa CA. Spray forming high-speed steel properties and processing. Mater Sci Eng, A 2004;383(1):87–95.
[18] Mesquita RA, Barbosa CA. High-speed steels produced by conventional casting, spray forming and powder metallurgy. Mater Sci Forum 2005:498. 499244-50.
[19] Igharo M, Wood JV. Investigation of M2 high speed steel produced by osprey process. Powder Metall 1989;32(2):124–31.
[20] Wang H, Hou L, Li Y, Ou P, Shen L, Wen X, et al. Effect of niobium on the secondary precipitates and tempering resistance of spray-formed M3:2 high-speed steel. J Mater Eng Perform 2019;28(2):1–12.
[21] Torres H, Varga M, Ripoll MR. High temperature hardness of steels and iron-based alloys. Mater Sci Eng, A 2016;671(1):170–81.
[22] Groche P, Moeller N, Hoffmann H, Suh J. Influence of gliding speed and contact pressure on the wear of forming tools. Wear 2011;271(9):2570–8.
[23] Casagrande A, Cammarota GP, Micele L. Relationship between fatigue limit and Vickers hardness in steels. Mater Sci Eng 2011;528(9):3468–73.
[24] Lee TL, Mi J, Zhao SL, Fan JF, Zhang SY, Kabra S, et al. Characterization of the residual stresses in spray-formed steels using neutron diffraction. Scripta Mater 2015:10082–5.
[25] Senthilvelan T, Raghukandan K, Venkatraman A. Testing and quality standards for powder metallurgy products. Mater Manuf Process 2003;18(1):105–12.
[26] Pippel E, Woltersdorf J, Pöckl G, Lichtenegger G. Microstructure and nanochemistry of carbide precipitates in high-speed steel S 6-5-2-5. Mater Char 1999;43(1):41–55.
[27] Di H, Zhang X, Wang G, Liu X. Spheroidizing kinetics of eutectic carbide in the twin roll-casting of M2 high-speed steel. J Mater Process Technol 2005;166(3):359–63.
[28] Ernst IC, Duh D. ESP4 and TSP4, a comparison of spray formed with powder metallurgically produced cobalt free high-speed steel of type 6W-5Mo-4V-4Cr. J Mater Sci 2004;39(22):6831–4.
[29] Chaus AS, Dománková M. Precipitation of secondary carbides in M2 high-speed steel modified with titanium diboride. J Mater Res 2013;22(5):1412–20.
[30] Hwang KC, Lee S, Lee HC. Effects of alloying elements on microstructure and fracture properties of cast high speed steel rolls Part II. fracture behavior. Mater Sci Eng 1998;254(1):282–95.
[31] Park JW, Huo CL, Lee S. Composition, microstructure, hardness, and wear properties of high-speed steel rolls. Metall Mater Trans 1999;30(2):399–409.
[32] Mesquita RA, Barbosa C, Gonçalves C, Slaviero A. Effect of hardening conditions on mechanical properties of high speed steels. Int Heat Treat Surf Eng 2011;5(1):36–40.
[33] Luo Y, Guo H, Sun X, Mao M, Guo J. Effects of austenitizing conditions on the microstructure of AISI M42 high-speed steel. Metals 2017;7(1):27.
[34] Liu B, Lu X, Pi Z, Jia C, Zheng W, Wu L, et al. Effect of quenching temperature on transformation mechanism of carbides of M42. Xiyou Jinshu Cailiao Yu Gongcheng/Rare Metal Materials and Engineering 2017;46(3):829–34.
[35] Moghaddam EG, Varahram N, Davami P. On the comparison of microstructural characteristics and mechanical properties of high-vanadium austenitic manganese steels with the Hadfield steel. Mater Sci Eng, A 2012:532260–6.
[36] Llorca J, Suresh S, Needleman A. An experimental and numerical study of cyclic deformation in metal-matrix composites. Metall Mater Trans 1992;23(3):919–34.
[37] Armas AF, Petersen C, Schmitt R, Avalos M, Alvarez-Armas I. Mechanical and microstructural behaviour of isothermally and thermally fatigued ferritic/martensitic steels. J Nucl Mater 2002;307(1):509–13.
[38] Sjöström J. Chromium martensitic hot-work tool steels : damage, performance and microstructure. Materialteknik; 2004.
[39] Medvedeva A, Bergstroem J, Gunnarsson S, Andersson J. High-temperature properties and microstructural stability of hot-work tool steels. Mater Sci Eng, A 2009;523(1–2):39–46.
[40] Kassner ME, Kumar P, Blum W. Harper-Dorn creep. Int J Plast 2007;23(6):980–1000.
[41] Park CP, Lee JJ, Kang SK, Kim YC, Woo KS, Jeon SW, et al. Evaluation of high-temperature Vickers hardness using instrumented indentation system. Mater Sci Eng, A 2015:65015–9.
[42] Tsui TY, Oliver WC, Pharr GM. Influences of stress on the measurement of mechanical properties using nanoindentation: Part I. Experimental studies in an aluminum alloy. J Mater Res 1996;11(3):752–9.
[43] Cheng YT, Cheng CM. Effects of 'sinking in' and 'piling up' on estimating the contact area under load in indentation. Phil Mag Lett 1998;78(2):115–20.
[44] Saha R, Nix WD. Effects of the substrate on the determination of thin film mechanical properties by nanoindentation. Acta Mater 2002;50(1):23–38.
[45] Xiao L, Ye D, Chen C. A further study on representative models for calculating the residual stress based on the instrumented indentation technique. Comput Mater Sci 2014;82(1):476–82.
[46] Moharrami R, Sanayei M. Developing a method in measuring residual stress on steel alloys by instrumented indentation technique. Measurement 2020:158107718–27.
[47] Moharrami R, Sanayei M. Numerical study of the effect of yield strain and stress ratio on the measurement accuracy of biaxial residual stress in steels using indentation. J Mater Res Technol 2020;9(3):3950–7.
[48] Chaus AS, Dománková M. Unknown high-speed steel. Mater Lett 2021;292(2057):129653.
[49] Nogueira RA, Ribeiro OCS, Neves d. Influence of the heat treatment on the microstructure of AISI T15 high speed steel. Mater Sci Forum 2003:416. 41889-94.
[50] Hetzner DW, Van Geertruyden W. Crystallography and metallography of carbides in high alloy steels. Mater Char 2008;59(7):825–41.
[51] Boccalini M, Goldenstein H. Solidification of high speed steels. Int Mater Rev 2001;46(2):92–115.
[52] Peng H, Hu L, Zhang X, Wei X, Li L, Zhou J. Microstructural evolution, behavior of precipitates, and mechanical properties of powder metallurgical high-speed steel S390 during tempering. Metall Mater Trans 2018;50(2):874–83.
[53] Ghomashchi MR, Sellars CM. Microstructural changes in as-cast M2 grade high speed steel during high temperature treatment. Met Sci 2013;18(1):44–8.
[54] Chaus AS, Rudnickii FI. Diffusion and secondary carbide precipitation in high-speed steels. Defect Diffusion Forum 2010:297. 3011071-6.
[55] Parabina GI, Yatsenko AS, Makogon VN, Marchenko LN, Mikhailov PI. Quality of commercial high-speed steel from powder metallurgy. Metallurgist 1986;30(3):86–7.